PCCP

PAPER

Temperature and pressure-induced strains in anhydrous iron trifluoride polymorphs†

Cite this: DOI: 10.1039/d0cp05888b

M. Recio-Poo,[a] A. Lobato,[a] A. Otero-de-la-Roza,[a] M. A. Salvadó,[a] M. E. Arroyo-de Dompablo[b] and J. M. Recio*[a]

Received 11th November 2020,
Accepted 7th January 2021

DOI: 10.1039/d0cp05888b

rsc.li/pccp

Various structural configurations of iron trifluoride appear at the nanoscale and macroscopic size, either in the amorphous or crystalline state. The specific atomic organization in these structures crucially alters the performance of FeF_3 as an effective cathode in Li-ion batteries. Our detailed first-principles computational simulations examine the structural strains induced by temperature and stress on the four anhydrous polymorphs observed so far in FeF_3 at ambient pressure. A wealth of data covering previous experimental results on their equilibrium structures and extending their characterization with new static and isothermal equations of state are provided. We inform on how porous apertures associated with the six-octahedra rings of the HTB and pyrochlore phases are modified under compressive and expansive strains. A quasi-auxetic behavior at low pressures for the ground state rhombohedral phase is detected, which is in concordance with its anomalous structural anisotropy. In contrast with the effect of temperature, this structure undergoes under negative pressure phase transitions to the other three polymorphs, indicating potential conditions where low-density FeF_3 could show a better performance in technological applications.

1 Introduction

Li-Ion batteries (LIBs) display many desirable features, which makes them the leading technology used in portable electronic devices and current hybrid and electric vehicles.[1–3] The importance of LIBs has motivated numerous investigations aimed at enhancing the electrochemical activity at the atomic, nano- and macroscopic scales of the materials involved in this technology. Transition metal fluorides are promising materials for use in LIB construction because they present a number of desirable characteristics (large electron exchange, highly ionic bonding, chemical stability, *etc.*) that makes their study interesting at the basic and applied level.[4,5] In particular, iron fluorides[6] have been the focus of recent attention for their application in LIBs (see ref. 4 and references therein).

The pioneer X-ray study conducted by Hepworth *et al.*,[7] and the subsequent neutron diffraction experiments by Wollan *et al.*,[8] provided the first unequivocal characterization of the antiferromagnetic rhombohedral unit cell of FeF_3. These initial structural determinations were followed by a number of reference investigations on the synthesis, structural and magnetic behavior of first-row transition metal trifluorides in the 1980s.[9–13] It has not been until the last two decades, when an increasing interest in this family of compounds has been renewed due to their outstanding performance as cathodes in LIBs. Anhydrous[14] and, more frequently, hydrated[15–17] FeF_3 polymorphs have been the subject of detailed electrochemical studies highlighting their advantages as cathode materials and proposing alternatives to overcome the inherent insulator character of this ionic compound. The theoretical specific capacity of FeF_3 is 712 mA h g^{-1} for the three-electron redox process Fe^{3+}/Fe^0. Reversible electrochemical activity (Li intercalation process followed by a conversion-type reaction) is reported in a wide voltage-range (1–4.5 V), resulting in specific capacities as high as 600 mA h g^{-1}.[14,15,18] However, the material suffers of poor capacity retention associated to structural degradation upon consecutive charge–discharge cycles.[19] The local atomic environments of the Fe and F atoms was shown to play a key role in how the cation insertion and conversion reactions enhance the charge/discharge capacity and the cycle stability of FeF_3-based electrodes.[15,17] In this regard, amorphous phases of FeF_3,[20] nanostructures displaying shorter Fe–F distances than in the crystalline materials,[21] and composites of $FeF_3{\cdot}0.33(H_2O)$ coated with MoO_3[17] or ball-milled with carbon[21,22] are specific examples where the correlation between the local atomic structure and electrochemical activity is apparent.

[a] MALTA Team and Departamento de Química Física y Analítica, Universidad de Oviedo, E-33006 Oviedo, Spain. E-mail: jmrecio@uniovi.es
[b] Departamento de Química Inorgánica, Universidad Complutense de Madrid, E-28040 Madrid, Spain

† Electronic supplementary information (ESI) available. See DOI: 10.1039/d0cp05888b

Q2 Table 1 Summary of structural parameters and Wyckoff positions of the FeF_3 polymorphs in their conventional unit cells. For the ReO_3-type structure, the parameters for the rhombohedral cell (Z = 2) are also given (details in the text)

	α	HTB	Pyr	ReO_3	
	Ref. 7	Ref. 9	Ref. 11	Ref. 24	
Space group	$R\bar{3}c$	$Cmcm$	$Fd\bar{3}m$	$Pm\bar{3}m$	$Pm\bar{3}m$
Z	2	12	16	1	2
a (Å)	5.362	7.423	10.325	3.857	5.455
b (Å)	5.362	12.730	10.325	3.857	5.455
c (Å)	5.362	7.526	10.325	3.857	5.455
α (°)	57.99	90.0	90.0	90.0	60.0
Fe_1	(2b) 0, 0, 0	(4b) 0, $\frac{1}{2}$, 0	(16c) 0, 0, 0	(1a) 0, 0, 0	0, 0, 0
Fe_2	—	(8d) $\frac{1}{4}$, $\frac{1}{4}$,0	—	—	
F_1	(6e) 0.839, 0.661, $\frac{1}{4}$	(8f) 0, 0.216, 0.551	(48f) 0.310, $\frac{1}{8}$, $\frac{1}{8}$	(3c) $\frac{1}{2}$, 0, 0	$\frac{3}{4}$, $\frac{3}{4}$, $\frac{1}{4}$
F_2	—	(16h) 0.188, 0.396, 0.043	—	—	—
F_3	—	(4c) 0, 0.529, $\frac{1}{4}$	—	—	—
F_4	—	(8g) 0.210, 0.218, $\frac{1}{4}$	—	—	—

Three polymorphs of anhydrous FeF_3 are known at ambient pressure, namely rhombohedral (r- or α-FeF_3), hexagonal tungsten bronze (HTB-FeF_3), and cubic pyrochlore (Pyr-FeF_3).[9,11,23] A fourth polymorph with a cubic ReO_3-type structure is obtained displacively from the rhombohedral phase.[11,24] Table 1 shows the unit cell parameters for these four structures. Which of the four polymorphs is experimentally observed depends on temperature and also on the method and experimental conditions of the synthesis. De Pape and Ferey[11] suggested that "the free enthalpy of the different forms of FeF_3 decreases in the order Pyr-HTB-α", with their volumes varying inversely to their thermodynamic stability. However, to the best of our knowledge, the verification of this statement and an understanding of the polymorphic stability in FeF_3 have not been reported in spite of the potential implications in the field of LIBs.

Theoretical calculations concerning polymorphism in FeF_3 are scarce. As far as we know, no computational study of the phase diagram has been conducted yet. Nevertheless, studies using *ab initio* approaches have been carried out for particular phases, mostly the α phase. The Li–Fe–F diagram has been studied computationally by Doe *et al.* using the rhombohedral cell.[26] A trirutile Li_xFeF_3 structure with $x \geq 0.2$ has also been explored with density-functional theory (DFT) in order to study Li insertion in FeF_3.[27] In addition, the electronic and magnetic properties of α-FeF_3 have been also calculated by Li *et al.*[18] Of relevance to our work is the first-principles calculation of the response to hydrostatic pressure in α-FeF_3, where this phase is found to be stable up to more than 50 GPa.[28] A computational study of the Ti doping effects in hydrated HTB-$FeF_3{\cdot}0.33H_2O$ has also been reported, which includes calculated structural, energetic, and electronic structure data of the HTB-FeF_3 phase.[16] The hydrated material keeps the same crystal structure as its anhydrous counterpart.[9] Similar information is provided by Li *et al.* as part of a theoretical simulation on how water content in the HTB-FeF_3 polymorph affects its performance as cathode in LIBs.[29] The effect of Ag decorating HTB-$FeF_3{\cdot}0.33H_2O$ on the band gap and electronic density of states of this polymorph has been also calculated using DFT by Li *et al.*[30] For Pyr-FeF_3, Amirabbasi *et al.*[31] have rigorously addressed its controversial magnetic behavior providing structural properties of positive and negative strained configurations by means of DFT calculations. We are not aware, however, of any other computational studies regarding the Pyrochlore and ReO_3-type polymorphs of FeF_3.

Given the interplay between macroscopic structure, polymorph stability, atomic environments, and the performance of FeF_3 as cathode in Li-ion batteries, we carried out a systematic investigation of polymorphism in this material. By macroscopic structures one should understand not only space group and unit cell changes under variable thermodynamic conditions, but also pore size, texture,[32] particle size and crystallinity[20] and coating using diverse chemical agents such as carbon (through black acetylene, functionalized graphene, carbon nanotubes, *etc.*)[14] or MoO_3.[17] However, we restrict this study to the four observed crystalline anhydrous structures, three of them (α, HTB, and Pyr) often discussed in the context of LIBs and energy storage. Our focus is on how strained configurations can be reached by modifying temperature and/or applying hydrostatic pressure. To this end, we calculate isothermal equations of state for the four polymorphs with an emphasis on the anomalous anisotropic behavior of the rhombohedral phase and the changes in pore apertures of the HTB and Pyr hexagonal-like channels. In addition, we provide for the first time thermodynamic conditions under which one of the four FeF_3 polymorphs is stable or may be found to be metastable. This constitutes a critical assessment of De Pape and Ferey stability conjecture.[11] It is to be noticed that a precedent investigation of our group contains a thorough analysis of the α-ReO_3-type transition in FeF_3.[33]

The paper is organized in three more sections. Next, we describe our computational modeling techniques and provide the parameters used in the calculations. The Results and discussion section is split into four subsections dealing, respectively, with the equilibrium structures, the isothermal equations of state, the structural anisotropy of α-FeF_3, and the phase stability. We finish summarizing the main findings and the conclusions of our investigation.

2 Computational details and modeling

In order to study the electronic structure and thermodynamic stability of FeF_3 polymorphs, total energy (E) calculations in a number of selected volumes (V) for each polymorph were performed using density-functional theory with a planewave-pseudopotential scheme as implemented in Quantum Espresso (QE).[34] The projector augmented wave (PAW) method was used,[37] and the B86bPBE functional for the exchange–correlation contribution[38] was chosen. $3d^6 4s^2$ and $2p^5$ electrons have been considered in the active valence space for Fe and F, respectively. A Hubbard-like energy term was included with a U parameter of 5 eV in order to treat the strong on-site Coulomb interaction of the d-electrons in iron,[39] similarly to the GGA+U calculations of Li *et al.* in the α phase.[18] The exchange-hole dipole-model[40,41] (XDM) model for van der Waals weak interactions has also been used with the canonical damping function parameters (a_1 = 0.6512 and a_2 = 1.4633 Å).

An analysis of how the total energy and stress tensor converge with the k-points grids in each phase and with plane-wave kinetic energy cutoff was carried out. A plane-wave kinetic energy cutoff of E_{cut} = 70 hartree ensures a convergence in the energy and stress tensor in the order of 10^{-5} hartree and 0.5 GPa, respectively. Fig. S1 in the ESI† displays the total energy (per unit formula) and stress tensor variation with uniform (Monkhorst–Pack[42]) k-point grids of various densities (a single value N represents a uniform[42] $N \times N \times N$ grid). The values chosen for the production calculations are shown in Table S1 of the ESI.†

Spin-polarized calculations were carried out to describe magnetism in FeF_3. A number of tests were performed to evaluate energy differences between different magnetic orderings and the non-magnetic state in α-FeF_3. We concluded that the ferromagnetic and the different antiferromagnetic orderings are not qualitatively different regarding polymorph stability. For example, relative energies between AF and FM orderings along a wide range of volumes are always lower than 0.005 hartree for the α phase. Slight quantitative differences appear for some properties of particular structures that will be further detailed if they are relevant to the discussion of our results. On the other side, the description of FeF_3 as non-magnetic (non-spin-polarized) yields unrealistic $E(V)$ curves, with differences with respect to AF and FM orderings as high as 0.1 hartree. Details of this analysis are collected in Fig. S2 of the ESI.† Based on this analysis, unless otherwise specified, the antiferromagnetic (AF) ordering has been used only for the α and ReO_3 phases of FeF_3, whereas the HTB and Pyr polymorphs (with more than two Fe atoms in the unit cell) are described as ferromagnetic (FM). For reference, the Néel temperatures of the α, HTB, and Pyr phases are equal to 365 K, 110 K, and 20 K, respectively.[11]

To take into account thermal effects under the so-called quasiharmonic approximation (QHA), evaluation of phonon dispersion curves for the α and ReO_3-type phases were carried out within the linear response perturbation scheme implemented in QE. These calculations were performed using the relaxed equilibrium geometries (maximum forces on atoms are lower than 10^{-4} hartree per bohr) obtained at the same volumes where the total energy was minimized. A grid of $2 \times 2 \times 2 \times$ vibrational q wavevectors was sampled in the first Brillouin zone. Unfortunately, due to the greater number of atoms in the corresponding unit cells, these QHA calculations lead to very time-consuming computations for the HTB and Pyr phases, and were not considered for them. By means of a computational cheaper alternative, the vibrational contributions to the internal energy were also evaluated for these HTB and Pyr phases using a simple Debye-like model. For the rhombohedral phase, the use of this simple model allows us to compare its performance with respect to the more accurate results obtained when the phonon dispersion curves are explicitly calculated.

Both schemes are implemented in the Gibbs code.[35,36] Numerical and analytical equations of state (EOS) were used to describe the computed (E, V) points of the four FeF_3 phases. Specifically, gibbs2 was used to determine their Vinet[44] isothermal EOS parameters (volume, V_0, bulk modulus, B_0, and its pressure derivative, B_0', all evaluated at zero pressure) at static and 300 K, and to calculate thermodynamic properties of all the polymorphs, including the phases' Gibbs free energy as a function of pressure and temperature. Details of these approaches and the computational strategy can be found elsewhere.[35,36,43]

3 Results and discussion

3.1 Structure at zero pressure static conditions

Fig. 1 displays the conventional and primitive unit cells of the α, HTB, Pyr and ReO_3-type polymorphs of FeF_3. The primitive unit cells vary from the conventional cells only in the HTB and Pyr phases. The primitive unit cells have rhombohedral, tetragonal, rhombohedral and cubic shapes for the α, HTB, Pyr and ReO_3 phases, respectively. For the ReO_3 phase, two different settings have been considered, namely cubic and rhombohedral. The use of two different settings allows the calculation of the FM and AF magnetic orderings. The AF ordering in the ReO_3 phase is calculated using the rhombohedral (Z = 2) cell, while the primitive cell is used for the FM ordering. The ReO_3 and α structures present a group–subgroup relationship. The cubic ReO_3 structure is obtained from the rhombohedral phase when $\alpha = 60^\circ$, $a_r = \sqrt{2} \times a_c$ (a_r and a_c are the unit cell parameters in the rhombohedral and cubic cells, respectively) and x = 0.75 is the atomic coordinate of the F atom. The cubic Z = 1

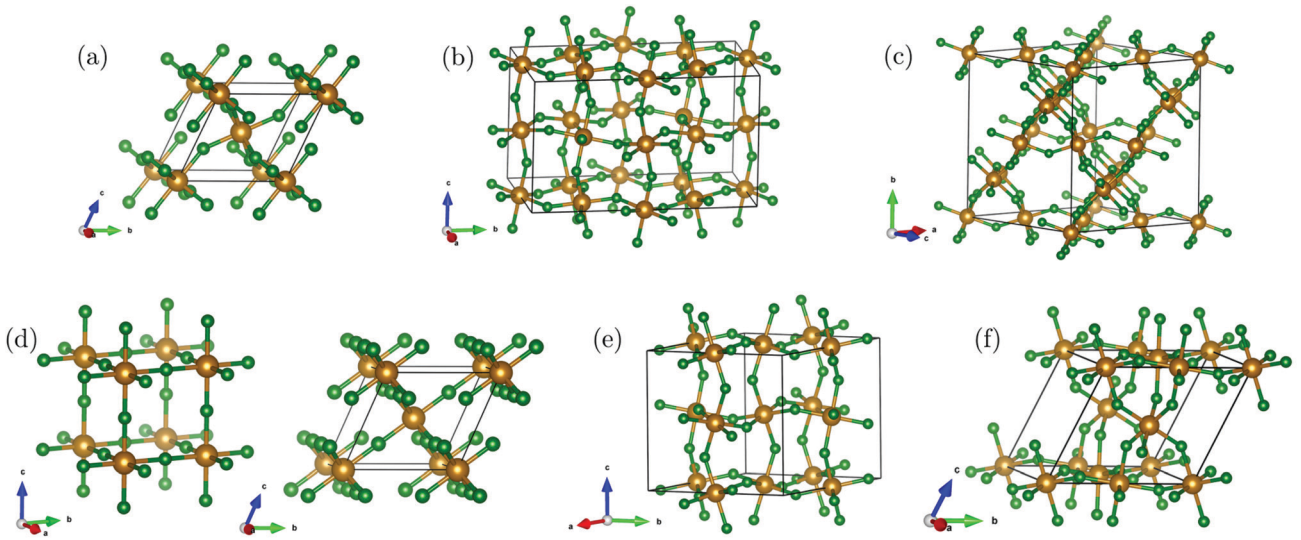

Fig. 1 Conventional cells of the α (a), HTB (b), Pyr (c), and ReO_3-type (d) structures. For the ReO_3 phase, the rhombohedral setting is also shown. HTB (e) and Pyr (f) primitive unit cells are also shown. Brown and white balls correspond to Fe and F atoms, respectively.

ReO_3 phase is a defective perovskite-like (ABX_3) structure with Fe and F atoms sitting respectively at the corners and edge centers of the cubic cell, whereas the A atom is missing. In Table 1, a detailed description including experimental values of the corresponding unit cells are collected.

The static energy-volume curves for the four FeF_3 polymorphs are displayed in Fig. 2. The volume range contains the experimental equilibrium volumes observed at room temperature. The α and cubic ReO_3 phases share the same energy curve at large volumes in both magnetic configurations, indicating a convergence between the two (red and black lines, respectively).

Table 2 gathers the calculated equilibrium zero-pressure parameters of the corresponding conventional unit cells (a, b, c, α), including atomic coordinates (x) and the relative energy of the other three polymorphs relative to the α phase (ΔE_0). These values are obtained after the Vinet fittings to the calculated points displayed in Fig. 2. In the α, HTB and Pyr structures, the number of atomic coordinates that are optimized in the energy minimizations is one, eight and one, respectively. For the sake of simplicity, the crystallographic coordinates of the four non-equivalent F atoms in the HTB structure are not collected in Table 2. Their optimized values and the experimental values

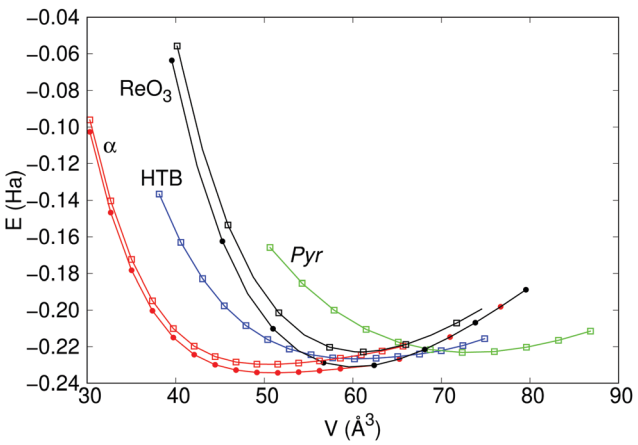

Fig. 2 Calculated $E(V)$ curves for the α, HTB, Pyr, and ReO_3 polymorphs. Solid circles and empty squares refer to AF and FM orderings, respectively.

Table 2 Summary of calculated zero-pressure static structural and energetic parameters of the FeF_3 polymorphs. SPG and Z stand, respectively, for the space group and number of formula units in each unit cell. a, b, c are the lattice parameters, x is the internal atomic coordinate of F, d(Fe–F) and δ are the F–F bond length and Fe–F–Fe bond angle, respectively, V_0 is the static equilibrium volume, and ΔE_0 is the energy difference with respect to the α phase at equilibrium, per unit formula. The atomic coordinates of the F atoms in the HTB structure are given in the text. Experimental data (when available) are displayed under each calculated value

	α		HTB	Pyr	ReO_3	
	FM	AF	FM	FM	FM	AF
SPG	$R\bar{3}c$	$R\bar{3}c$	$Cmcm$	$Fd\bar{3}m$	$Pm\bar{3}m$	$Pm\bar{3}m$
Z	2	2	12	16	1	2
a (Å)	5.422	5.421	7.516	10.537	3.941	5.536
	—	5.362[7]	7.423[9]	10.325[11]	3.877[24]	5.483[24]
b (Å)	5.422	5.421	12.799	10.537	3.941	5.536
	—	5.362[7]	12.730[9]	10.325[11]	3.877[24]	5.483[24]
c (Å)	5.422	5.421	7.529	10.537	3.941	5.536
	—	5.362[7]	7.526[9]	10.325[11]	3.877[24]	5.483[24]
α (°)	55.9	56.0	90.0	90.0	90.0	60.0
	—	57.9[45]	90.0	90.0	90.0	60.0
x	0.879	0.874	[a]	0.313	0.5	0.75
	—	0.839[7]	[a]	0.310[31]	0.5	0.75
d(Fe–F) (Å)	1.969	1.964	1.972	1.974	1.970	1.957
	—	1.923[45]	1.947[9]	1.927[11]	—	1.939[46]
δ (degree)	141.1	142.4	145.0	140.2	180.0	180.0
	—	152.1[11]	149.8[9]	142.3[31]	—	180.0
V_0 (Å^3)	50.3	51.1	60.4	73.2	61.2	60.0
	—	51.9[11]	59.3[11]	68.8[11]	58.3[24]	58.3[24]
ΔE_0 (kJ mol^{-1})	—	—	11.4	16.0	17.5	10.5

are, respectively: F(8f) (0, 0.2190, 0.5584) and (0, 0.2156, 0.5511), F(16h) (0.1853, 0.3959, 0.0542) and (0.1876, 0.3963, 0.0434), F(4c) (0, 0.5474, 0.25) and (0, 0.5286, 0.25), and F(8g) (0.20389, 0.2115, 0.25) and (0.2101, 0.2176, 0.25). The overall agreement with the experimental data is very good: our GGA+U calculations lead to structural parameters and equilibrium volumes consistent with observed values (a slight overestimation is in line with typical results using GGA functionals[18]).

Our results verify the correlation between energy and volume predicted by De Pape and Ferey:[11] ΔE_0 and V_0 increase along the sequence α, HTB, Pyr. We confirm that the α polymorph is the thermodynamically stable phase of anhydrous FeF_3, and it has the highest density. The distortion from the ideal ReO_3 cubic symmetry lowers the energy by 17.5 kJ mol^{-1} (FM) or 10.5 kJ mol^{-1} (AF) at these static conditions. Differences with respect to HTB and Pyr phases are of the same order.

Fig. 3 shows a polyhedral-style view along the three crystallographic axes of the primitive unit cells for the α, HTB, Pyr, and ReO_3 structures. The building blocks are FeF_6 polyhedra linked by F atoms. α and ReO_3 structures present 4-membered octahedral rings leading to the formation of empty channels with rhombic-shape apertures. These channels are 3D-like, as they are present in the three considered perpendicular projections (Fig. 3(a) and (d)). Moreover, since the three views are equal, only one is displayed for each of these two polymorphs. In these polyhedral representations, the relationship between α and ReO_3 structures is clearly illustrated and consists of a tilting mechanism of the rigid FeF_6 octahedra that leads to rhombic channels all with the same aperture in the ReO_3 structure. On the other hand, HTB and Pyr polymorphs present 6-membered octahedral rings that give rise to hexagonal channels (Fig. 3(c) and (d)). For the HTB structure, these empty hexagonal channels are only present when following one precise orientation. They are thus referred to as 1D channels. On the contrary, the Pyr structure channels are 3D-like, being connected in the three perpendicular orientations. Therefore, packing efficiency decreases from the α and ReO_3 structures to the HTB and Pyr phases. This feature has been shown to anti-correlate with a better performance in the Li-insertion process,[15] since the ion mobility improves as the size of the aperture and the dimensionality of the channels increase.

For HTB and Pyr polymorphs, Fig. 4 shows the hexagonal channels in detail. The size of the channel apertures, Φ, can be evaluated using the following expression:[15]

$$\Phi = D_{FF} - 2r_w(F), \quad (1)$$

where D_{FF} is the average distance between fluorine atoms along the diagonals, and $r_w(F)$ is the van der Waals fluorine radius (1.47 Å) quoted in ref. 47. For the HTB phase, the D_{FF} calculated value of 5.69 Å leads to a channel aperture of 2.75 Å, a value consistent with previous computational[16,29] and experimental data.[11] For the Pyr polymorph, the calculated average distance between the diagonal F atoms of the channels is 5.42 Å, which yields an aperture value of 2.48 Å, also in very good agreement with the reported experimental data in ref. 15. In spite of the lower value for the Pyr structure, this phase shows a better performance for the insertion process as the network of channels is three-dimensional.

3.2 Static and thermal equations of state

Temperature and hydrostatic pressure induce homogenous strains in crystalline solids. The response of the structure to these perturbations is in general anisotropic due to its symmetry and the spatial configuration of atoms and bonds. Fig. 5 shows how volume and bond lengths and angles of the four polymorphs evolve as pressure is applied at static and 300 K conditions. Thermal contributions have been taken into account by means of the explicit calculation of the phonon

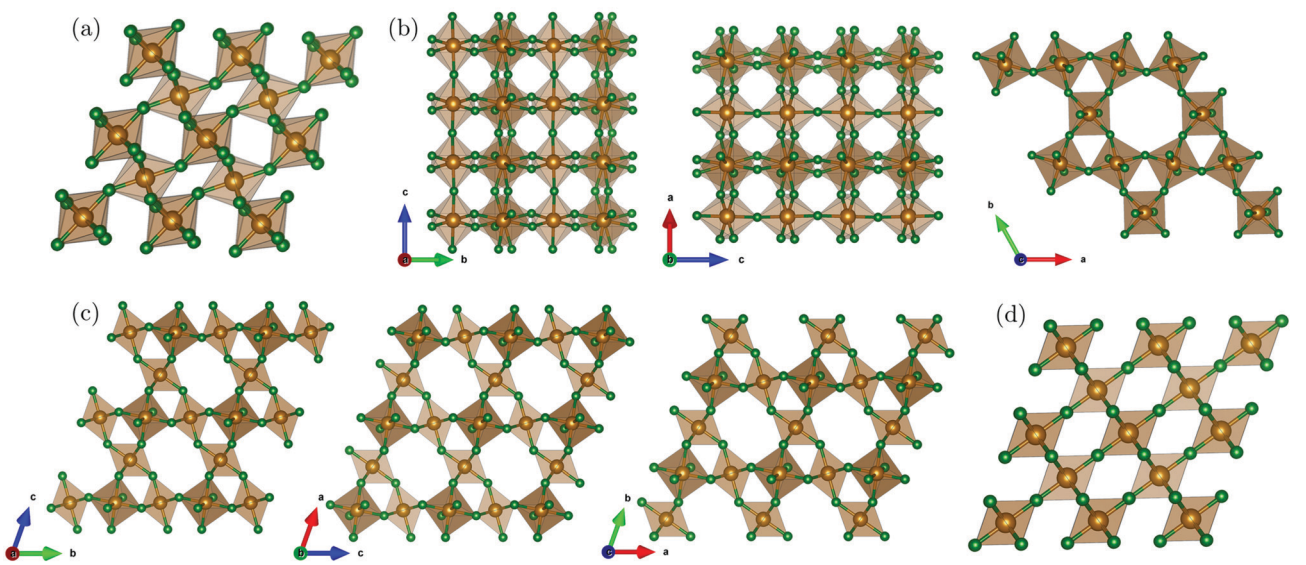

Fig. 3 Polyhedral projections along the three crystallographic axes of the primitive unit cells of the α (a), HTB (b), Pyr (c) and ReO_3 (d) structures. For the α and ReO_3 phases only one of the three equivalent views is displayed.

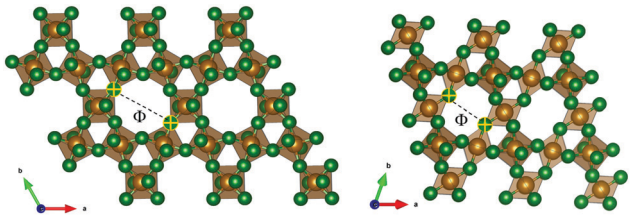

Fig. 4 View of the hexagonal cavities formed in HTB (left) and Pyr (right) phases, highlighting their dimensions (Φ). We have used the van der Waals radius (1.47 Å) from ref. 47) for the fluorine atom.

density of states under the QHA in the α phase, whereas the much simpler Debye model was used in the other phases. Except for the ReO_3-type structure, the main volume reduction and subsequent densification is not achieved by a decreasing of nearest neighbor distances, but by the rotations of the octahedral FeF_6 units that behave according to the so-called rigid unit model.[48] This can be seen from the very low slope of the d_{Fe-F} curves in contrast with the greater decrease of the Fe–F–Fe bond angle curve.

The same compression mechanism has already been extensively analyzed using experimental and theoretical data by Zhu *et al.*[28] and was also reported in the experimental works of ref. 45 and 46 for the α-FeF_3 phase. Interestingly enough, our results show that an analogous behavior is observed in the HTB and Pyr polymorphs too, although the distinctive roles under compression of the bond length and the bond angle is not so clear in the cubic Pyr phase. In the ReO_3 structure, symmetry forces the bond angle to have a 180° value and the effect of pressure leads exclusively to a reduction of the volume of the octahedral units. As a result of these mechanisms, a high compressibility is expected for the α, HTB, and Pyr phases, whereas the compressibility of the ReO_3-type phase should be lower as well as explicitly informative of the Fe–F bond strength. B_0 values collected in Table 3 confirm our expectations. Vinet EOS yields similar B_0 values below 50 GPa for the α, HTB and Pyr phases, whereas in the ReO_3 phase B_0 is around 100 GPa. We observe the expected decreasing in B_0 and increasing in B_0' when T increases. Discrepancies between previous reported experimental values[46] in the α phase (B_0 = 14(1) GPa, B_0' = 12(1)) and our calculated EOS parameters are partially solved when comparing with the calculated EOS parameters at 300 K. It is also to be noticed that B_0 and B_0' are correlated parameters in the non-linear analytical fittings, and if the previous reported value of B_0' decreases (usually lower values are reported), the mismatch between experimental and calculated B_0 values would decrease too. This is what is observed when the corresponding normalized volumes at 300 K are

Table 3 Calculated Vinet-EOS parameters of FeF_3 polymorphs at static conditions (first row), 300 K (second row)

	α		HTB	Pyr	ReO_3	
	FM	AF	FM	FM	FM	AF
B_0 (GPa)	35.0	30.3	40.7	48.7	103.3	99.4
	27.5	24.7	28.2	47.2	97.7	87.2
B_0'	4.97	8.16	4.90	2.27	3.77	4.65
	6.79	8.76	5.54	2.31	3.81	4.90

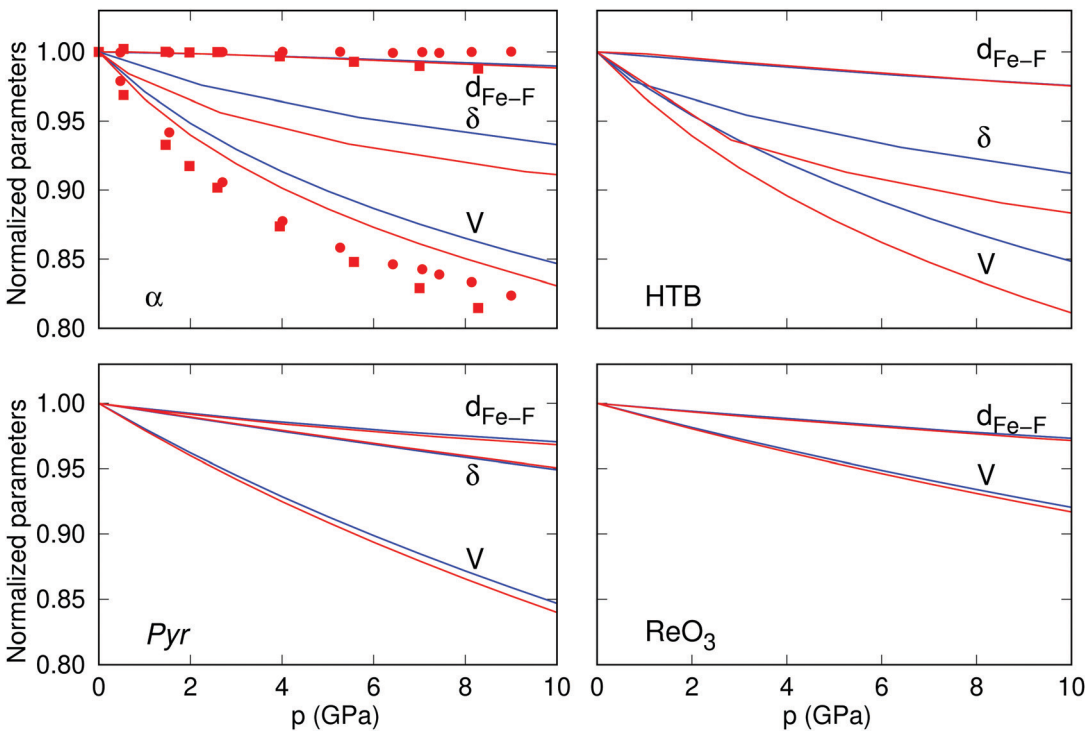

Fig. 5 Evolution with pressure of the normalized volume (V/V_0), Fe–F distance (d_{Fe-F}), and F–Fe–F angle (δ) in the FeF_3 polymorphs calculated at static (blue) and 300 K (red). Symbols stand for the experimental values of Sowa *et al.*[45] (squares) and Jørgensen and Smith[46] (circles).

represented in Fig. 5, though we are aware that our simulations tend to overestimate the cohesion of the α-FeF_3 phase.

By fine tuning pressure and temperature, we can access to atomic configurations displaying sensitive modifications of the pore apertures calculated at static conditions. As the HTB and Pyr phases are the ones with greater values, we have quantitatively analyzed the rates at which the diameters (D_{FF}) and apertures (Φ) of these phases change with p and T. Our results show the expected trends with these variables. Thus, for the HTB polymorph D_{FF} and Φ decreasing (p) and increasing (T) rates are, respectively, -3.44×10^{-2} Å GPa^{-1} and 6.18×10^{-4} Å K^{-1}. Lower values, but of the same order, are found for the Pyr structure: -5.09×10^{-2} Å GPa^{-1} and 1.68×10^{-4} Å K^{-1}. This information may be relevant to evaluate the convenience of applying thermal effects on these polymorphs when higher cations, as Na^+ and K^+, are involved in alkaline-ion batteries. Notice that, for instance, at 300 K the increase in the diameter of the pore aperture of the HTB structure is similar to the difference between Li^+ and Na^+ ionic radii.

3.3 Uncommon structural anisotropy in the α phase

Our calculations accurately capture the experimental d_{Fe-F} pressure trend in the α phase. Interestingly, it is only in this structure where we have a lower negative value for the slope computed at 300 K than at static conditions. This surprising result evidences an anomalous structural anisotropic behavior of α-FeF_3. In fact, a negative thermal expansion was experimentally reported for the c lattice parameter when its unit cell is expressed in the hexagonal setting.[12] Moreover, c has been also observed to slightly increase in the pressure range up to 10 GPa.[28,45,46] The combined thermal and pressure effects on c affects d_{Fe-F} and explains why the Fe–F bond is less compressible as temperature increases. To support this conclusion, we verify in Fig. 6 that our calculations reproduce the structural anisotropy observed in the α phase. Negative ($V/V_0 < 0$) and positive ($V/V_0 > 0$) strained structures correspond, respectively, to increasing pressure and temperature conditions.

Since the c lattice constant presents this unusual behaviour, it is appealing to evaluate the Poisson ratio (ν_{ij}) involving the c axis direction of this α phase to check if a negative value, characteristic of auxetic behavior is obtained here. Poisson's ratio is a dimensionless second-order tensor whose elements are defined in an isotropic medium as the negative of the quotient between the relative transverse strain (ε_j) induced by a relative longitudinal strain (ε_i):[49]

$$\nu_{ij} = -\frac{\varepsilon_j}{\varepsilon_i}, \quad (2)$$

where i and j are orthogonal lattice parameters. In this definition, the Poisson ratio was implicitly assumed to be positive if the transverse and longitudinal strains have different signs, which is the most common behavior. However, there are materials that expand their transverse dimension when subjected to a longitudinal tensile stretching and decrease it when

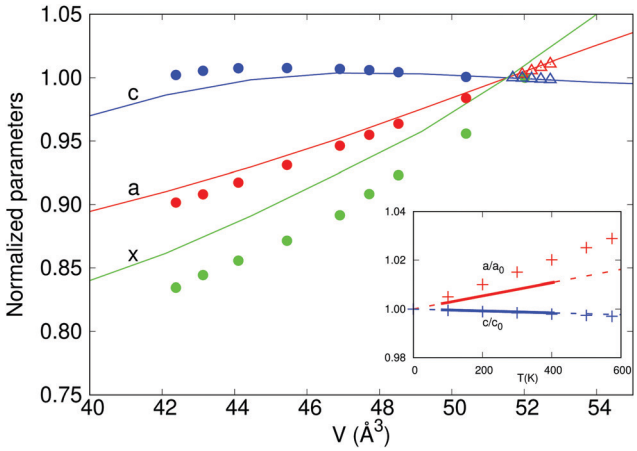

Fig. 6 Evolution with volume of calculated lattice parameters a and c and the atomic coordinate of the F atom (x) in the hexagonal setting of the α-FeF_3 polymorph. Circles and triangles stand for the experimental values reported by Jorgensen and Smith[46] and Leblanc *et al.*,[12] respectively. All values normalized by the corresponding equilibrium values at static conditions (calculations), zero pressure (circles) and lowest measured temperature (triangles). The inset displays the temperature evolution of normalized a and c lattice parameters (hexagonal setting) according to the empirical linear fitting of ref. 12 (dashed (extrapolated) and continuous line) and our calculation (crosses).

compressed.[50] In this way, they present a negative Poisson ratio. These materials receive the name of auxetics and present enhanced mechanical properties such as shear, indentation and fracture resistance.[49] The allowable range for ν_{ij} in an isotropic medium is, according to the theory of elasticity, between +0.5 (liquid state) and −1.0 (infinitely compressible solid).[51]

To evaluate the Poisson ratio of α-FeF_3, the E–a–c potential energy surface (PES) was computed in a grid of 10c values and 12a values containing the equilibrium lattice parameters (Fig. 7(a)). Due to the anomalous c parameter behavior, our focus is on the particular coefficient obtained after stretching the crystal along the c direction (ν_{ca}). We observe that this longitudinal strain $\varepsilon_c = \frac{c - c_0}{c_0}$ induces a transverse (slightly negative) strain $\varepsilon_a = \frac{a - a_0}{a_0}$ which results in a low Poisson ratio, $\nu_{ca} = -\varepsilon_a/\varepsilon_c$, of less than 0.09. In the projected 2D surface (Fig. 7(b)), the slight negative slope of the darkest region illustrating the lowest energy region can be used to anticipate a positive value of ν_{ca}. For a quantitative evaluation of this parameter, an analytical function was fitted to the computed data points. Details of the fitting procedure are given in the ESI† (Table S2 and Fig. S3, ESI†). The PES was replicated with this function at different pressures up to 10 GPa by simply adding the corresponding pV term at each node of the grid. Transverse strains induced by longitudinal strains were computed on these enthalpy surfaces to evaluate Poisson ratios at different pressures and static conditions. It is interesting to notice that ν_{ca} decreases to a value close to zero at around 3 GPa, but without reaching negative values (Fig. 7(c)) and then increases in the 0–10 GPa pressure range.

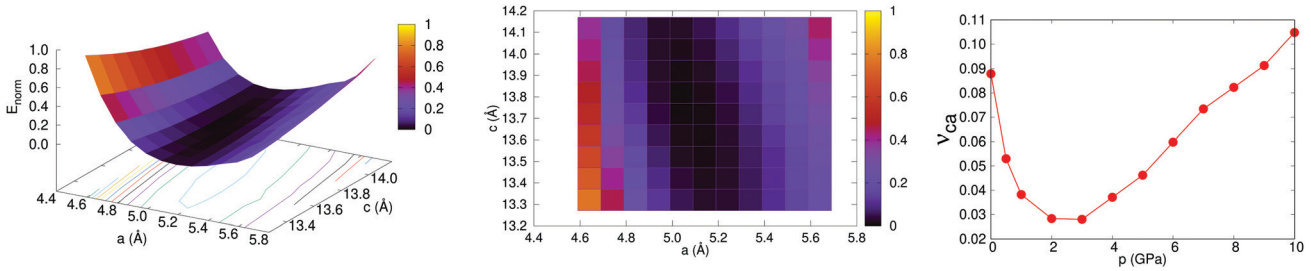

Fig. 7 (a) Energy–a–c 3D potential energy surface of the rhombohedral α phase under static conditions. (b) 2D projection on the a–c surface. Color code is for normalized energies going from 0 (darkest color) to 1 (lightest colour). (c) Pressure evolution of the Poisson coefficient when stretching the crystal along the c direction.

3.4 Phase stability under negative pressure conditions

At a given pressure and temperature, the local minima of the non-equilibrium Gibbs free energy G^*:[36]

$$G^*(V(\vec{x}); p, T) = E_{\text{sta}}(V(\vec{x})) + pV + F^*_{\text{vib}}(V(\vec{x}); T) \qquad (3)$$

are associated with different polymorphs of a crystalline system. Among all these minima, the one with the lowest G^* value represents the thermodynamically stable phase. In the above equation, $\vec{x}$ contains the structural parameters and atomic coordinates, and F^*_{vib} is the vibrational Helmholtz free energy accounting for all thermal contributions. At zero pressure and static conditions, G^* is simply the static energy. For this reason, and by means of Fig. 2, we can state that α is the stable phase at such conditions, with the rest being potential metastable phases.

Fig. 8 displays the temperature evolution at p = 0 of the calculated Gibbs free energy (*i.e.* the Helmholtz free energy) for the α, HTB and Pyr polymorphs in their ferromagnetic states. These calculations were carried out adding the Debye thermal contributions to the calculated (E_i, V_i) data points, as implemented in the gibbs2 code. The Vinet EOS was chosen for fitting the initial ($E_i - V_i$) data points.

Since the computed Gibbs free energy functions do not cross at any point within the considered temperature range, it is to be concluded that, within the Debye approach, is not possible to predict any temperature-induced phase transitions between these structures. In this way, at zero pressure, the rhombohedral α structure remains as the thermodynamic stable phase for all temperature values. However, the $E - V$ calculated curves (Fig. 2) suggest the existence of phase transitions at increasing volumes.

At zero pressure static conditions, HTB and Pyr equilibrium volumes are, respectively, 60.4 Å^3 and 73.2 Å^3, and their corresponding equilibrium energies are above the value of the α phase (Table 2 and Fig. 2). The figure allows tracing tangent lines with positive slopes connecting the α and HTB, and the α and Pyr energy-volume curves. Common tangent slopes identify negative values of the transition pressure (p_{tr}) in the static limit. Therefore, we expect negative p_{tr} values for both α-HTB and α-Pyr transformations. In each transition, the volume of the final phase is unequivocally greater than that of the α phase, thus yielding positive transition volumes. This

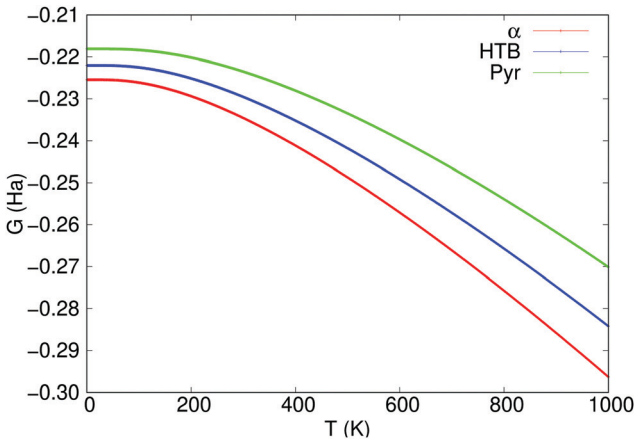

Fig. 8 Evolution with temperature of calculated Gibbs energies for α, HTB and Pyr FeF_3 phases.

discontinuity in the volume at the (negative) transition pressure is a sign of a first-order character. Furthermore, we can also predict a less negative p_{tr} value for α-Pyr than for α-HTB transition, according to a careful inspection of their common tangent slopes.

Fig. 9 shows the differences in the calculated static Gibbs free energy (*i.e.* enthalpy) of the two metastable phases with respect to the FM-α structure. Transition pressures are obtained when such differences become zero ($G_A(p_{\text{tr}}) = G_B(p_{\text{tr}})$). The p_{tr} values obtained for the α-HTB and α-Pyr transitions are, respectively, −1.3 GPa and −1.05 GPa. Since the curves for HTB and Pyr phases intersect at less negative pressure than these two values, our calculations predict just one phase transition from α to Pyr polymorph at −1.05 GPa, being Pyr the stable phase from that point on. This −1.05 GPa pressure yields a ΔV_{tr} = 22.6 Å^3, similar to the value at zero pressure static conditions (22.0 Å^3). At the α-Pyr transition pressure, the HTB phase is only 5 × 10^{-4} hartree (1.56 kJ mol^{-1}) above, thus showing a clear competition between these two phases at this negative pressure value. It is therefore pertinent to notice that, if kinetic effects hinder the α-Pyr transition, the HTB structure would appear as metastable at −1.3 GPa, involving a lower ΔV_{tr} value of 10.4 Å^3. We should also indicate that these kinetic effects become more important when temperature is low and, therefore, HTB could

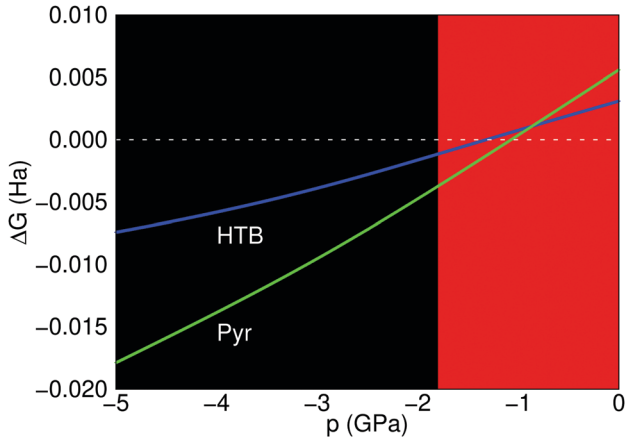

Fig. 9 Gibbs free energy difference between α (horizontal zero value line) and HTB and Pyr phases at static conditions. The vertical line at −1.8 GPa value representing the pressure where the α structure (red) becomes the ReO_3 phase (black) according to results of our previous investigation.[33]

be favoured at low temperatures under this negative pressure conditions.

Regarding the transition between the group–subgroup related α and ReO_3 phases, we refer to a precedent investigation were the strains inducing the thermodynamic or kinetic control of the transformation were analyzed in detail. As noticed in the caption of Fig. 9, a negative pressure of −1.8 GPa indicates the boundary between the α and ReO_3-type structures according to our previous calculations.[33]

It is also important to note that the negative transition pressure values found in our calculations are not necessarily related with temperature-induced transitions. Actually, we have shown before that at zero pressure, a temperature-induced transition from the α to the HTB, Pyr or ReO_3 phase is not predicted according to our $G(T)$ Debye-like calculations. Conversely, the potential emergence of new phases under negative pressures is revealed. Negative pressures are associated with positive strain effects produced by novel techniques of fabrication of cathode materials, such as epitaxial growth and nanoparticle formation.[52–54] In both cases, interatomic distances greater than in equilibrium bulk configurations can be found as a consequence of using substrates with lattice parameters larger than those corresponding to the synthesized material or due to the lower coordination presented in the surface of the nanoparticles.

In FeF_3, experimental results in finite nanocrystals samples of 18 nm size[55] can be interpreted as due to strained surface configurations behaving similarly to α-FeF_3 at negative pressures. Indeed, albeit other factors may also apply, the XRD patterns of these nanocomposites are indexed using the ReO_3-type structure, which is the phase found in our simulations at −1.8 GPa. This effect could be amplified during epitaxial growth experiments, although it has not been studied yet to the best of our knowledge. Positive strain effects due to epitaxial growth or nanoparticle formation can also result into phase transitions as it has been observed in $CsPbX_3$ (X = Cl, Br, I) halide perovskites[56–58] where the archetypical ReO_3-type cubic phase is found. We believe that our results could open new routes to explore how the ground state rhombohedral FeF_3 phase evolves to the lower dense polymorphs (HTB, Pyr), which are the phases showing better performance as positive electrodes in LIBs.

4 Conclusions

Our first-principles calculations predict that zero pressure energies and volumes increase along the sequence α-HTB–Pyr, thus confirming an old conjecture raised by De Pape and Ferey in 1986.[11] Under compressive strains, the HTB and Pyr structures behave following the same mechanism as previously found in the rhombohedral phase: volume reductions are mainly due to F–Fe–F bond angle changes and not to shortening of Fe–F bond lengths. This is a distinctive feature of these soft and flexible networks that display bulk moduli lower than 50 GPa. Notice that for the less compressible ReO_3 structure, the reduction of volume informs directly on the Fe–F bond strength. Quasi-auxetic behavior detected in the α phase evidences anomalous Fe–F bond length changes and uncommon anisotropy under pressure and temperature. For the HTB and Pyr structures, we have explored how the hexagonal-like pore apertures are modified by negative and positive strains with rates of -3.44×10^{-2} Å GPa^{-1}, 6.18×10^{-4} Å K^{-1} and -5.09×10^{-2} Å GPa^{-1}, 1.68×10^{-4} Å K^{-1}, respectively. This information has implications on the potential use of other alkaline metals in ion-based batteries.

Our Debye-like model does not predict any T-induced transition between α, HTB and Pyr polymorphs. Negative pressures, on the other hand, inform of conditions where the Pyr phase is found with lower enthalpy than the rhombohedral structure. Moreover, since the transition volume accompanying this reconstructive transition is higher than 22 $Å^3$, a high energy barrier along the α-Pyr transition path is expected. This fact could facilitate the appearance of the HTB polymorph at a lower negative pressure where its enthalpy is in between the values of the α and Pyr structures. All these calculations reveal that FeF_3 polymorphs show atomic networks sensitive to moderate changes of pressure and temperature. Strain tuning using these two variables can lead to a variety of atomic configurations either continuously or disruptively if a phase transition takes place. Although hydrated polymorphs are more realistic for battery applications, we conclude that computational simulations of their anhydrous counterparts provide not only the understanding but also the precise thermodynamic conditions for selecting the appropriate pore apertures and the most suitable iron trifluoride structure to be used in high-performance ion battery and other technological applications.

Conflicts of interest

Q6

Acknowledgements

This work was supported by Spanish MCIU and MINECO through the following projects: PGC2018-094814-B-C2, PGC2018-097520-A-100, RyC-2016-20301, and RED2018-102612-T. Funding was also provided by FICYT-Principado de Asturias (Spain) under Project No. FC-GRUPIN-IDI/2018/000177. MALTA-Consolider supercomputing center is gratefully acknowledged.

References

1 P. G. Bruce, B. Scrosati and J.-M. Tarascon, Nanomaterials for rechargeable lithium batteries, *Angew. Chem., Int. Ed.*, 2008, **47**, 2930.

2 J. Cabana, L. Monconduit, D. Larcher and M. R. Palacin, Beyond intercalation-based Li-ion batteries: the state of the art and challenges of electrode materials reacting through conversion reactions, *Adv. Mater.*, 2010, **22**, E170.

3 N. Nitta, F. Wu, J. T. Lee and G. Yushin, Li-ion battery materials: present and future, *Mater. Today*, 2015, **18**, 252.

4 V. Murugesan, *et al.*, Lithium Insertion Mechanism in Iron Fluoride Nanoparticles Prepared by Catalytic Decomposition of Fluoropolymer, *ACS Appl. Energy Mater.*, **2**, 1832.

5 S. Tawa, Y. Sato, Y. Orikasa, K. Matsumoto and R. Hagiwara, Lithium fluoride/iron difluoride composite prepared by a fluorolytic sol-gel method: Its electrochemical behavior and charge-discharge mechanism as a cathode material for lithium secondary batteries, *J. Power Sources*, 2019, **412**, 180.

6 H. Arai, S. Okada, Y. Sakurai and J. Yamaki, Cathode performance and voltage estimation of metal trihalidesi, *J. Power Sources*, 1997, **68**, 716.

7 M. A. Hepworth, K. H. Jack, D. Peacock and G. J. Westland, The Crystal Structures of the Trifluorides of Iron, Cobalt, Ruthenium, Rhodium, Palladium and Iridium, *Acta Crystallogr.*, 1957, **10**, 63.

8 K. O. Wollan, H. R. Child, W. C. Koehler and M. K. Wilkinson, Antiferromagnetic Properties of the Iron Group Trifiuorides, *Phys. Rev.*, 1958, **112**, 1132.

9 M. Leblanc, G. Ferey, P. Chevallier, Y. Calage and R. De Pape, Hexagonal tungsten bronze-type Fe(III) fluoride:$(H_2O)_{0.33}$ FeF_3; crystal structure, magnetic properties, dehydration to a new form of iron trifluoride, *J. Solid State Chem.*, 1983, **47**, 53.

10 G. Ferey, M. Leblanc, R. D. Pape and J. Pannetiei, *Inorganic Solid Fluorides*, ed. P. Hagenmuller, Academic Press, Orlando, 1985.

11 R. de Pape and G. Ferey, A new form of FeF_3 with the pyrochlore structure: Soft chemistry synthesis, crystal structure, thermal transitions and structural correlations with the other forms of FeF_3, *Mater. Res. Bull.*, 1986, **21**(21), 971.

12 M. Leblanc, R. De Pape, G. Ferey and J. Pannetier, Ordered magnetic frustration-V. Antiferromagnetic structure of the hexagonal bronzoid HTB FeF_3; Comparison with the non frustrated rhombohedral form, *Solid State Commun.*, 1986, **58**, 171.

13 Y. Calage, M. Zemirli, J. M. Greneche, F. Varret, R. D. Pape and G. Fereyi, Mössbauer study of the new pyrochlore form of FeF_3, *J. Solid State Chem.*, 1987, **69**, 197.

14 S.-T. Myung, S. Sakurada, H. Yashiro and Y.-K. Sun, Iron trifluoride synthesized via evaporation method and its application to rechargeable lithium batteries, *J. Power Sources*, 2013, **223**, 1.

15 L. Liu, H. Guo, M. Zhou, Q. Wei, Z. Yang, H. Shu, X. Yang, J. Tan, Z. Yan and X. Wang, A comparison among $FeF_3.3H_2O$, $FeF_{3.0}{\cdot}33H_2O$ and FeF_3 cathode materials for lithium ion batteries: Structural, electrochemical, and mechanism studies, *J. Power Sources*, 2013, **238**, 501.

16 Z. Yang, Z. Zhang, Y. Yuan, Y. Huang, X. Wang, X. Chen and S. Wei, First-principles study of Ti doping in $FeF_3{\cdot}0.33H_2O$, *Curr. Appl. Phys.*, 2016, **16**, 905.

17 X. Zhou, J. Ding, J. Tang, J. Yang, H. Wang and M. Ji, Tailored MoO_3-encapsulated $FeF_3{\cdot}0.33H_2O$ composites as high performance cathodes for Li-ion batteries, *J. Electroanal. Chem.*, 2019, **847**, 113227.

18 R. F. Li, S. Q. Wu, Y. Yang and Z.-Z. Zhu, Structural and electronic properties of Li-ion battery cathode material FeF_3, *J. Phys. Chem. C*, 2010, **114**(39), 16813.

19 K. Shimoda, M. Shikano, M. Murakami and H. Sakaebe, Capacity fading mechanism of conversion-type FeF3 electrode: Investigation by electrochemical operando nuclear magnetic resonance spectroscopy, *J. Power Sources*, 2020, **47**, 228772.

20 D. Dambournet, M. Duttine, K. W. Chapman, A. Wattiaux, O. Borkiewicz, P. J. Chupas and A. Demourgues, and H-Groulti, Resolving and Quantifying Nanoscaled Phases in Amorphous FeF_3 by Pair Distribution Function and Mössbauer Spectroscopy, *J. Phys. Chem. C*, 2014, **118**, 14039.

21 N. Yamakawa, M. Jiang, B. Key and C. P. Grey, Identifying the local structures formed during lithiation of the conversion material, iron fluoride, in a Liion battery: a solid-state NMR, X-ray diffraction, and pair distribution function analysis study, *J. Am. Chem. Soc.*, 2009, **131**, 10525.

22 F. Badway, F. Cosandey, N. Pereira and G. G. Amatucci, Carbon metal fluoride nanocomposites: High-capacity reversible metal fluoride conversion materials as rechargeable positive electrodes for Li batteries, *J. Electrochem. Soc.*, 2003, **150**, A1318.

23 N. Louvain, A. Fakhry, P. Bonnet, M. El-Ghozzi, K. Guérin, M.-T. Sougrati, J.-C. Jumas and P. Willmann, One-shot *versus* stepwise gas–solid synthesis of iron trifluoride: investigation of pure molecular F2 fluorination of chloride precursors, *Cryst. Eng. Commun.*, 2013, **15**, 3664.

24 A. Tressaud, J.-M. Dance, F. Ménil, J. Portier and P. Hagenmulleri, Non-Stoechiométrie dans le Système FeF_3 WO_3, *Z. Anorg. Allg. Chem.*, 1973, **399**, 231.

25 NIST standard reference database, https://www.nist.gov/srd, 31/08/2020.

26 R. E. Doe, K. A. Persson, Y. S. Meng and G. Ceder, First-Principles Investigation of the Li–Fe–F Phase Diagram and Equilibrium and Nonequilibrium Conversion Reactions of Iron Fluorides with Lithium, *Chem. Mater.*, 2008, **20**, 5274.

27 Y. Zheng, R.-F. Li, S.-Q. Wu, Y.-H. Wen, Z.-Z. Zhu and Y. Yang, First-Principles Investigation on the Lithium Ion Insertion/Extraction in Trirutile Li$_x$FeF$_3$, *Electrochemistry*, 2013, **81**, 12.

28 F. Zhu, X. Lai, X. Wu, Y. Li and S. Qin, Experimental and theoretical investigation on the compression mechanism of FeF$_3$ up to 62.0 GPa, *Acta Crystallogr.*, 2014, **70**, 801.

29 Z. Li, B. Wang, C. Li, J. Liu and W. Zhang, Hydrogen-bonding-mediated structural stability and electrochemical performance of iron fluoride cathode materials, *J. Mater. Chem. A*, 2015, **3**, 16222.

30 Y. Li, X. Zhou, Y. Bai, G. Chen, Z. Wang, H. Li, F. Wu and C. Wu, Building an electronic bridge *via* Ag decoration to enhance kinetics of iron fluoride cathode in lithium-ion batteries, *ACS Appl. Mater. Interfaces*, 2017, **9**, 19852.

31 M. Amirabbasi, N. Rezaei, M. Alaei, F. Shahbazi and H. Akbarzadeh, Crossover between tricritical and Lifshitz points in pyrochlore FeF$_3$, *Phys. Rev. B*, 2019, **100**, 054441.

32 K. Guérin, *et al.*, Rhombohedral iron trifluoride with a hierarchized macroporous/mesoporous texture from gaseous fluorination of iron disilicide, *Mater. Chem. Phys.*, 2016, **173**, 355.

33 A. Lobato, M. Recio-Poo, A. Otero-de-la-Roza, M. A. Salvadó and J. M. Recio, Controlling anion off-center positions through thermodynamics and kinetics in flexible perovskite-like materials, *Phys. Chem. Chem. Phys.*, in press.

34 P. Giannozzi, *et al.*, QUANTUM ESPRESSO: a modular and open-source software project for quantum simulations of materials, *J. Phys.: Condens. Matter*, 2009, **21**, 395502.

35 A. Otero de la Roza and V. Luaña, Gibbs2: A new version of the quasi-harmonic model code. I. Robust treatment of the static data, *Comput. Phys. Commun.*, 2011, **182**, 1708.

36 A. Otero de la Roza, D. Abbasi-Pérez and V. Luaña, Gibbs2: A new version of the quasiharmonic model code. II. Models for solid-state thermodynamics, features and implementation, *Comput. Phys. Commun.*, 2011, **182**, 2232.

37 G. Kresse and D. Joubert, From ultrasoft pseudopotenitals to the projector augmented-wave method, *Phys. Rev. B: Condens. Matter Mater. Phys.*, 1999, **59**, 1758.

38 J. P. Perdew, J. A. Chevary, S. H. Vosko, K. A. Jackson, M. R. Pederson, D. J. Singh and C. Fiolhais, Atoms, molecules, solids, and surfaces: Applications of the generalized gradient approximation for exchange and correlation, *Phys. Rev. B: Condens. Matter Mater. Phys.*, 1992, **46**, 6671.

39 S. L. Dudarev, G. A. Botton, S. Y. Savrasov, C. J. Humphreys and A. P. Sutton, Electron-energy-loss spectra and the structural stability of nickel oxide: An LSDA+*U* study, *Phys. Rev. B: Condens. Matter Mater. Phys.*, 1998, **57**, 1505.

40 A. D. Becke and E. R. Johnson, Exchange-hole dipole moment and the dispersion interaction revisited, *J. Chem. Phys.*, 2007, **127**, 154108.

41 A. Otero de la Roza and E. R. Johnson, van der Waals interactions in solids using the exchange-hole dipole moment model, *J. Chem. Phys.*, 2012, **136**, 174109.

42 H. J. Monkhorst and J. D. Pack, Special points for Brillouin-zone integration, *Phys. Rev. B: Condens. Matter Mater. Phys.*, 1976, **13**, 5188.

43 J. M. Recio, J. M. Menéndez and A. Otero de la Roza, *An Introduction to High-Pressure Science and Technology*, CRC Press, Boca Raton, Florida, 2015.

44 P. Vinet, J. H. Rose, J. Ferrante and J. R. Smith, Universal features of the equation of state of solids, *J. Phys.: Condens. Matter*, 1989, **1**, 1941.

45 H. Sowa and H. Ahsbahs, Pressure-induced octahedron strain in VF$_3$-type compounds, *Acta Crystallogr., Sect. B: Struct. Sci.*, 1998, **54**, 578.

46 J.-E. Jørgensen and R. I. Smith, On the compression mechanism of FeF$_3$, *Acta Crystallogr., Sect. B: Struct. Sci.*, 2006, **62**, 987.

47 A. van Bondi, van der Waals volumes and radii, *J. Phys. Chem.*, 1964, **68**, 441.

48 M. T. Dove, *Introduction to Lattice Dynamics*, Cambridge University Press, Cambridge, 1993.

49 A. Yeganeh-Haeri, D. J. Weidner and J. B. Parise, Elasticity of α-cristobalite: A silicon dioxide with a negative Poisson's ratio, *Science*, 1992, **257**, 650.

50 V. H. Carneiro, J. Meireles and H. Puga, Auxetic materials – A review, *Mater. Sci.-Pol.*, 2013, **31**, 561.

51 A. H. Love, *A treatise on the mathematical theory of elasticity*, Dover, New York, 1944.

52 L. A. Bendersky, H. Tan, K. B. Karappanan, Z.-P. Li and A. C. Johnston-Peck, Crystallography and Growth of Epitaxial Oxide Films for Fundamental Studies of Cathode Materials Used in Advanced Li-Ion Batteries, *Crystals*, 2017, **7**, 127.

53 T. Kim, W. J. Jae, H. Kim, M. Park, J.-M. Han and J. Kim, A cathode material for lithium-ion batteries based on graphitized carbon-wrapped FeF$_3$ nanoparticles prepared by facile polymerization, *J. Mater. Chem. A*, 2016, **4**, 14857.

54 M.-J. Lee, S. Lee, P. Oh, Y. Kim and J. Cho, High Performance $LiMn_2O_4$ Cathode Materials Grown with Epitaxial Layered Nanostructure for Li-Ion Batteries, *Nano Lett.*, 2014, **14**(2), 993.

55 H. J. Tan, H. L. Smith, L. Kim, T. K. Harding, S. C. Jones and B. Fultz, Electrochemical Cycling and Lithium Inserction in nanostructured FeF$_3$ cathodes, *J. Electrochem. Soc.*, 2014, **161**, A445.

56 L. Protesescu, S. Yakunin, M. I. Bodnarchuk, F. Krieg, R. Caputo, C. H. Hendon, R. X. Yang, A. Walsh and M. V. Kovalenko, Noanocrystals of cesium lead halide perovskites (CsPbX$_3$, X = Cl, Br, and I): novel optoelectronic materials showing bright emission with wide color gamut, *Nano Lett.*, 2015, **15**, 3692.

57 J. Chen, Y. Fu, L. Samad, L. Dang, Y. Zhao, S. Shen, L. Guo and S. Jin, Vapor-phase epitaxial growth of aligned nanowire networks of cesium lead halide perovskites (CsPbX$_3$, X = Cl, Br, I), *Nano Lett.*, 2017, **17**, 460.

58 J. Song, J. Li, X. Li, L. Xu, Y. Dong and H. Zeng, Quantum Dot Light-Emitting Diodes Based on Inorganic Perovskite Cesium Lead Halides (CsPbX$_3$), *Adv. Mater.*, 2015, **27**, 7162.

Dear Author

Please use this PDF proof to check the layout of your article. If you would like any changes to be made to the layout, you can leave instructions in the online proofing interface. First, return to the online proofing interface by clicking "Edit" at the top page, then insert a Comment in the relevant location. Making your changes directly in the online proofing interface is the quickest, easiest way to correct and submit your proof.

Please note that changes made to the article in the online proofing interface will be added to the article before publication, but are not reflected in this PDF proof.